arXiv:1501.03130v2 [cond-mat.mtrl-sci] 4 Oct 2016

Crossover Behavior in the Packing and Assembly of Multivalent Lock-and-Key Colloids

N. Khalid Ahmed,[1] Greg van Anders,[1] Elizabeth R. Chen,[1,2] and Sharon C. Glotzer[1,3]

[1]*Department of Chemical Engineering, University of Michigan, Ann Arbor, MI 48109-2136, USA*
[2]*School of Engineering and Applied Sciences, Harvard University, Cambridge, Massachusetts 02138, USA*
[3]*Department of Materials Science and Engineering, University of Michigan, Ann Arbor, MI 48109-2136, USA*

(Dated: October 5, 2016)

Emergent behaviors occur in a vast array of systems across many scales, and are of fundamental physical importance because of the intrinsic difficulty in linking microscopic system properties to macroscopic behaviors. Here we study the emergent self-assembly behavior of model systems of recently synthesized families of concave dimpled hard spheres, or lock-and-key colloids. We find that as dimple size increases each family exhibits a crossover from a structure that does not reflect the particle symmetry to one that does and, surprisingly, the point at which this crossover occurs is approximately independent of the particle symmetry. Using a combination of numerical and analytic techniques we study systems at infinite and finite pressure, and find different common control parameters in each limit. Our results suggest there exists a set of experimentally realizable colloidal systems that exhibit complex emergent behaviors that can be traced to a common underlying microscopic control parameter.

I. INTRODUCTION

Physical systems from flocking animals [1] to heavy fermion materials [2] exhibit emergent macroscopic behaviors that are intrinsically difficult to predict from their microscopic properties [3]. Colloidal systems are fertile ground for investigating emergent behaviors for three reasons: a wide range of colloidal systems manifest emergent behaviors because they have entropy-driven phase behavior [4–6]; there is a broad range of techniques for manipulating colloids experimentally [7–9]; and colloidal systems can be investigated with a variety of techniques including *in situ* confocal microscopy [10]. Here, we study how microscopic properties affect the emergent macroscopic behavior of a model family of anisotropically shaped colloidal particles.

Anisotropic colloids that exhibit emergent directional entropic forces (DEFs) [5] when crowded in a thermal system are entropically patchy particles.[11] Entropic patches are shape features that promote local packing into target motifs and drive systems to order globally at high density.[11] Previously, we found that global ordering across a variety of systems was consistent with entropic patch strengths on the order of a few $k_B T$.[5, 11] However, if we desire particles with entropic patches of this strength, we do not currently have a complete set of rules for understanding how the particle geometry needs to be controlled to get them.[12] Due to the emergent nature of the underlying mechanism, establishing quantitative control is difficult.[5, 11, 12] Because of this difficulty, the rules we previously proposed for controlling DEFs were heuristic.[11] Here, we attempt to make the rules for controlling emergent DEFs more quantitative for a specific case of families (see Fig. 1) of anisotropic lock-and-key colloids [13].

Lock-and-key colloids are a convenient model system for investigating how to use geometry to control DEFs. More importantly, a number of theoretical [14–18] and experimental investigations [13, 19–26] have shown that lock-and-key colloids can form interesting structures, and recently synthesized families of multiply dimpled particles [19, 24] have not been previously simulated. Here, we use computer simulation and analytic calculations to study both packing (infinite pressure) and assembly (finite pressure) behaviors of families of multiply-dimpled particles that differ by dimple number and symmetry as a function of dimple size. We find that in both cases there are common, approximate microscopic parameters, based on particle geometry, that correlate with changes in bulk system behavior. However, the microscopic parameters are different in the dense packing and assembly limits. In the dense packing limit, a combination of analytic and numerical calculations show that (i) as dimple size increases, there is a crossover from body-centered-cubic (BCC) or -tetragonal (BCT) phases to phases that reflect the number of dimples and particle symmetry, and surprisingly (ii) this point of crossover occurs approximately independent of particle symmetry and

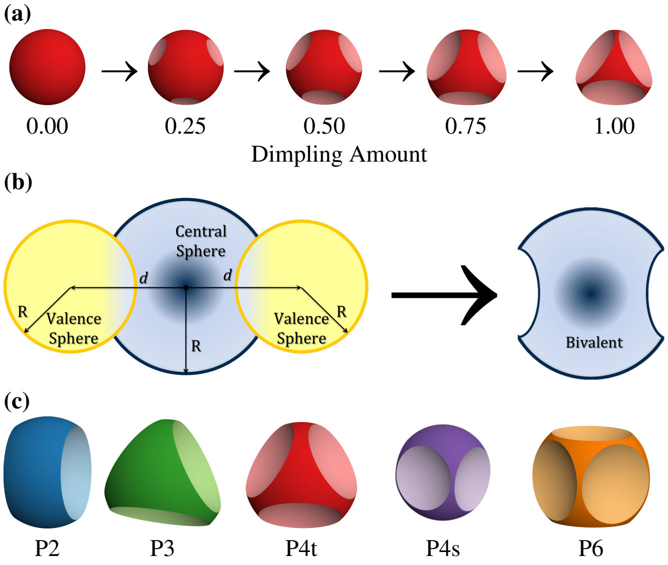

FIG. 1. (a) Change in shape of a tetrahedral tetravalent particle from convex to concave as dimpling amount is increased from 0 to 1. (b) Parameterization of dimpled concave spheroidal particles. (c) Bivalent, trivalent, tetrahedral tetravalent, square tetravalent and hexavalent model spheroidal particles.

number of dimples. Similarly, in the assembly limit, we find that as dimple size increases in each family there is (i) a crossover from the face-centered-cubic (FCC) structures that are characteristic of hard sphere assembly [27] to BCC structures that are characteristic of soft sphere assembly [28], followed by (ii) a second crossover from BCC to behavior that is determined by the particle symmetry and number of dimples. Surprisingly (iii) this second point of crossover also depends on a quantity that is approximately independent of particle symmetry, though it is different from the control parameter in the dense packing limit. We find that in the dense packing limit, the crossover in behavior is determined by a quantity that depends simultaneously on the geometry of all of the particle features, whereas in the assembly limit it is determined by the volume of individual dimples. We interpret these results in light of previous work [5] arguing that shape entropy maximization causes entropically driven colloidal systems to optimize local packing. Our results provide detailed quantitative evidence on how shape features control the macroscopic phase behavior of colloidal systems, while providing a concrete example of a set of experimentally realizable systems exhibiting changes in emergent macroscopic behaviors that are correlated with changes in a common microscopic control parameter.

II. MODEL AND METHODS

A. Model Systems

Particles, shown schematically in Fig. 1(c) and denoted by Pn_D, are made of a central sphere P that is symmetrically dimpled by subtracting n_D valence spheres, all of the same radius as the central sphere (hereafter taken to be one). The valence sphere positions are chosen to be related by discrete symmetries, and are equidistant from the central sphere as shown in Fig. 1(b). The use of equal radii suggests a connection between the dimple volume and free volume gained by the rest of the system when particles bind entropically [5, 11] due to shape complementarity. We study five families of particles that satisfy two criteria: they are multi-dimpled (so that we can differentiate between effects that are driven by individual shape features and effects that are driven by overall particle shape) and have discrete symmetries that are commensurate with some lattice symmetry group. We denote the particles as: bivalent (P2), trivalent (P3), tetrahedrally tetravalent (P4t), square tetravalent (P4s), and hexavalent (P6). For each of these concave particles, there is a one-parameter family of shapes determined by the distance d between the central and valence spheres which is maximum when the valence spheres are tangent to the central sphere and minimum when the valence spheres are tangent to each other.

TABLE I. Particles from the Concave Spheres Family

Particle	Description	Arrangement	Domain	Dimpling Amount
P2	Bivalent	Linear	$1 \leq d^2 \leq 4$	$\frac{(4-d^2)}{3}$
P3	Trivalent	Triangular	$\frac{4}{3} \leq d^2 \leq 4$	$\frac{3(4-d^2)}{8}$
P4t	Tetravalent	Tetrahedral	$\frac{3}{2} \leq d^2 \leq 4$	$\frac{2(4-d^2)}{5}$
P4s	Tetravalent	Square	$2 \leq d^2 \leq 4$	$\frac{(4-d^2)}{2}$
P6	Hexavalent	Cube	$2 \leq d^2 \leq 4$	$\frac{(4-d^2)}{2}$

Dimples are pairs of spherical caps bounded by the intersection of the central and valence spheres, and have the following volume, surface area, and circumference:

$$\begin{aligned} v_d &= \frac{\pi}{12}(d+4)(2-d)^2 \, , \\ s_d &= \pi(2-d) \, , \\ c_d &= \pi\sqrt{4-d^2} \, . \end{aligned}$$

B. Overlap Algorithm for Dimpled Spheres

Standard methods (see, e.g., [29]) for determining the overlap between anisotropic bodies rely on convexity. Previous theoretical work on concave particles in 3D [15, 16, 30, 31] used modifications of an overlap algorithm introduced by He and Siders [32] that required the radius of the valence sphere to be smaller or equal to the parent sphere and the particles were restricted to one valence sphere, $(n_D = 1)$. For the multi-dimpled particles we study here, we use a recently developed overlap algorithm [33]. The algorithm [33] is a recursive algorithm based on the Cayley-Menger volume determinant and similar dihedral angle determinants. This overlap algorithm considers all topological types of overlap among the spheres and calculates the mutual union and the mutual intersection among them.

C. Dense Packing

We vary the square of the distance between the centers of the central and the valence spheres d^2 in increments of 0.01 for each of the particles, as shown in Table I. The domain for d varies between particles, so we normalize by linearly mapping d^2 to the "dimpling amount" f, where $f = 0$ $(f = 1)$ when d^2 is maximum (minimum).

We construct dense packings of multi-dimpled particles numerically following a standard protocol used in several other recent studies [34–39]. The densest packing structure is found by compressing systems with up to eight particles placed in a box with periodic boundary conditions [35, 39]. Isobaric (NPT) simulations, in which the box is allowed to take the shape of an arbitrary parellelepiped, are then run with a slowly increasing pressure. Each system is compressed 400 times, and the densest packing overall is recorded.

As has been done previously for particles of other shape, [35, 39] where tractable, we use numerical putative densest packings as *ansatzes* for analytical packing constructions, which can be used to compute exact dense packing curves.

We identify crystal structures by replacing each particle by a point at its centroid as in several previous works [11, 36–38, 40].

D. Self Assembly

We study the self assembly of multi-dimpled particles with MC simulations using techniques from several other recent studies [5, 11, 34–39]. We use isochoric (NVT) MC simulations with periodic boundary conditions to study systems of N particles, with N ranging from 512 to 2064. These system sizes are typical of recent work examining entropy driven self assembly of hard shapes (e.g. [11, 34, 36, 37]) Each system is initially equilibrated as a dense, metastable fluid for 10^5 MC sweeps. Isochoric (NVT) simulations are then performed where the packing fraction is slowly increased until it reaches a target value. The system is then allowed to equilibrate at this state point for $\sim 5\times10^8$ MC sweeps. Equilibration times were chosen based on typical equilibration times that have been observed in other studies of hard shapes [34, 36], as their assembly originates in similar entropic forces. [5] A few experiments were also performed to $\sim 10^{10}$ MC sweeps to verify that despite their concave shape, no nucleation or crystal growth is found to occur beyond typical equilibration times for hard convex particles. Densities are varied between $0.25 \leq \phi \leq \phi^*$, where ϕ^* is the densest known packing fraction for that particle. A full MC sweep for a system of N particles consists of $N+1$ trial moves including arbitrary translation, rotation, and box shearing moves. Maximum step sizes are periodically adjusted to keep the acceptance probabilities at 30%. To check each self-assembled structure for equilibration, we allow the system to evolve over time scales that are at least an order of magnitude larger than the time scale for nucleation and growth, and longer than system auto-correlation times. All findings are verified by running independent simulations with different initializations and in different box sizes. The assemblies reported are those that form at the minimum density.

III. RESULTS AND DISCUSSION

A. Densest Packings

Following [36, 39, 41], we study continuous shape deformations. We compute putative densest packings for each family of particles at 100 different dimpling amounts $f \in [0,1]$; see Fig. 2. To verify the putative densest packings predicted numerically via MC simulations in this section, we perform analytic packing calculations for our particles (see appendix C). We find that our numerical calculations match very well with the analytic findings, with an error less than 0.001%.

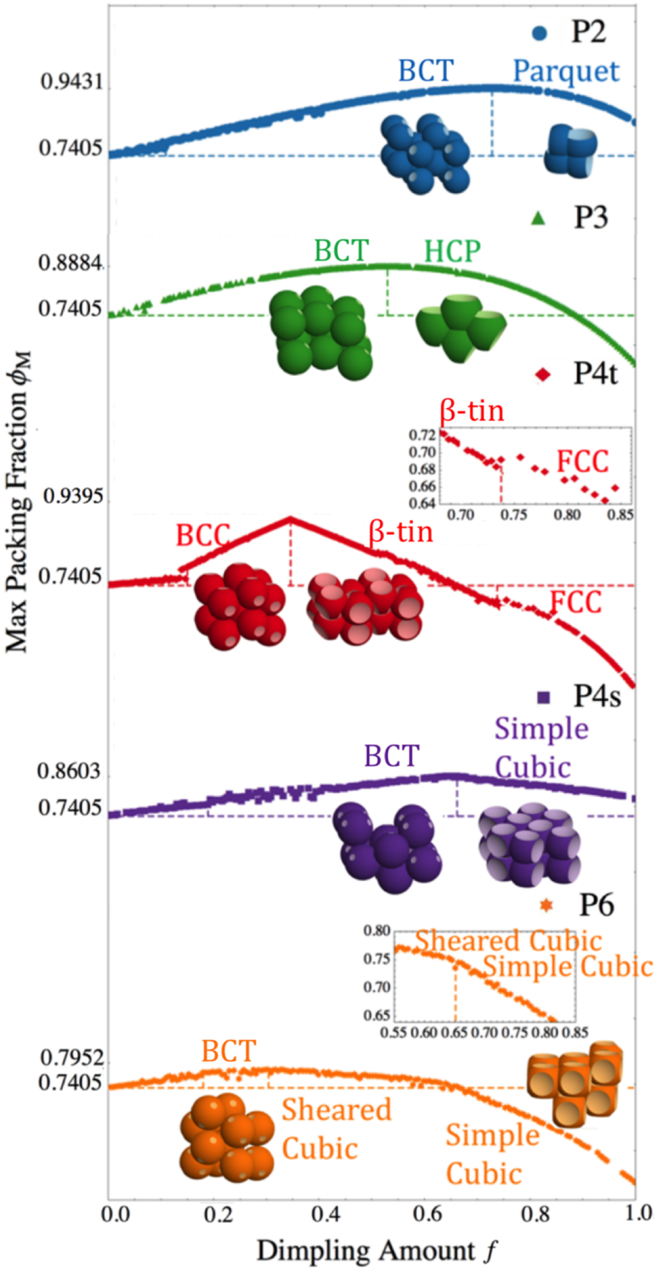

FIG. 2. Numerical calculations of the density ϕ of the densest obtained packing for dimpled particles as a function of dimpling amount f. The curves for different particles are shifted along the y-axis for clarity. Packing fraction is maximum at a critical dimpling amount $f = f^*_{DP}$ when the dominating features switch from convex to concave regions of the particles. For small f, particles shear from a thermodynamic preference for FCC packing in the hard sphere limit to a BCT packing with the introduction of dimpling. This is not smoothly captured in numerical calculations, but we show that the transition is smooth through analytic packing calculations. (Right Insets) For P4t and P6 particles, a second transition at larger f is seen from β-tin to FCC and sheared cubic to simple cubic respectively.

1. FCC–BCT Transition

In all cases, for small $f \approx 0$, particles pack most densely into FCC lattices, like hard spheres [27]. For slightly larger values $f \leq f^*_{DP}$, all particle types pack like soft spheres [37] into a BCT structure. This transition from FCC to BCT packing structures stems from a new contact between particles upon dimpling, dimple-sphere contact, in addition to sphere-sphere contact. The dimple-sphere contact reduces the contact distance between neighboring particles. This results in a BCT structure with $\alpha = \beta \neq \gamma$, where α, β, and γ are lattice distances. The transition from FCC to BCT structures occurs almost instantaneously with dimpling, and is captured in our analytic densest packing calculations. We represent this with a single continuous curve in our analytic calculations in Figs. 10-14. However, in numerical putative densest packing calculations, the particles pack in the FCC structure until a large enough dimpling amount due to local frustrations. At these values of f, the dimples become increasingly filled by adjacent particles with decreasing system volume, allowing denser packings without the need for global structural rearrangement.

2. Critical Dimpling Amount

We observe a maximum in the densest packing curve of each family at a different critical dimpling amount f^*_{DP}. In each family, below the critical dimpling amount $f < f^*_{DP}$ particle dimples make contact with the convex part of adjacent particles. At $f > f^*_{DP}$, neighboring particles interlock within each other resulting in a crossover to a structure determined by the number and arrangement of dimples on individual particles. Coincident with the change in the contact between particles is a crossover in global structure from BCT structures to structures that depend on the number and arrangement of the concave particle features. Despite an apparent geometric similarity in the nature of the crossover, i.e. in each case the crossover is from BCT to a symmetry dependent structure, the point at which the crossover occurs, $f = f^*_{DP}$, varies by approximately a factor of two across particle types. This variation suggests that the dimpling amount f is not a well-chosen parameter for understanding the origin of the structural crossover. Instead, we find that the quantity

$$C_d = \frac{n_D c_d}{2\pi d}\,, \tag{1}$$

where n_D is the number of dimples, c_d is the dimple circumference, and d is the dimple depth, is in the range $C^*_d = 1.23 \pm 0.06$ at the crossover across particle types. We note that the dependence of this quantity on n_D, as well as c_d and d, suggests that the crossover is driven by changes in the geometry of the entire particle, and contrasts with what we find for self-assembly in section III B below.

We find that just above f^*_{DP}, P2 particles pack into a parquet structure (BCC without shearing); P3 particles pack into an AB-stacked hexagonal packing (hexagonal close packing–HCP); P4t particles pack into a β-tin lattice (sheared diamond); P4s particles pack into a tetragonal lattice with rotational parquet symmetry; and P6 particles pack into a simple cubic lattice. A further increase in f beyond f^*_{DP} introduces larger voids between particles and a reduction in packing fraction. As f increases beyond f^*_{DP}, dimple volume continues to increase, resulting in a smaller volume of the particle in the unit cell structure. This change results in a reduction in the packing density of these structures. At sufficiently large values of f, P3, P4t, and P6 particles pack less densely than spheres.

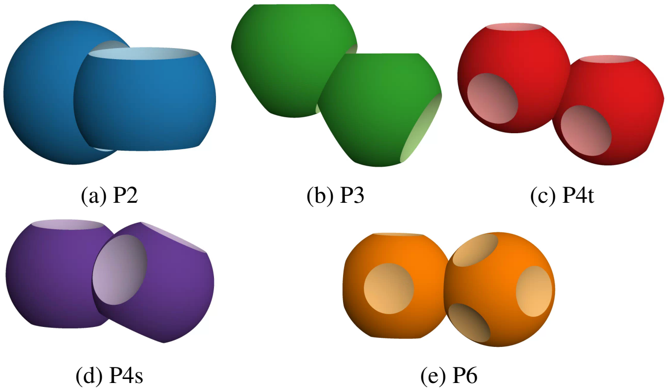
(a) P2 (b) P3 (c) P4t

(d) P4s (e) P6

FIG. 3. Configuration of neighboring particles at the critical dimpling amount for densest packing. We observe that the densest packing configuration is determined by a competition of the circumference and depth of the dimples.

For P2, P3, and P6 particles the packing fraction changes smoothly as a function of f about its maximum at f^*_{DP}; whereas for P4t and P4s particles there is a cusp. Both types of behavior have been observed previously in dense packings of continuously varying shapes [36, 39, 41]. For P2, P3, and P6 particles, the smooth behavior occurs because structures on either side of f^*_{DP} are related by a continuous shear. For P4t particles the cusp is the result of a crossover from BCC to β-tin, and for P4s it is the result of a change from BCC to simple cubic with a rotational parquet symmetry in the simple cubic lattice, which cannot be obtained by a simple shear from the BCC structure.

For P4t particles at high dimpling amounts, $f = 0.7374$, we find another transition from β-tin to FCC, shown in the first right inset of Fig. 2. At these large dimpling amounts, the densest packing structure arises from a competition between the parallel and anti-parallel alignment of the dimples. With increased dimple size, neighboring particles find more room to rotate while they are interlocked. This results in a denser packing when the dimples align parallel to each other instead, resulting in a transition from β-tin, where dimples exhibit anti-parallel alignment, to the FCC structure.

Similar to P4t particles, we find another transition for P6 particles at $f = 0.6510$, shown in the second right inset of Fig. 2. The particles transition from a sheared cubic arrangement to a simple cubic arrangement. This transition is observed in hexavalent particles because of their ability to shear along the 110 lattice vector direction, while neighboring particles remain interlocked in the same configuration.

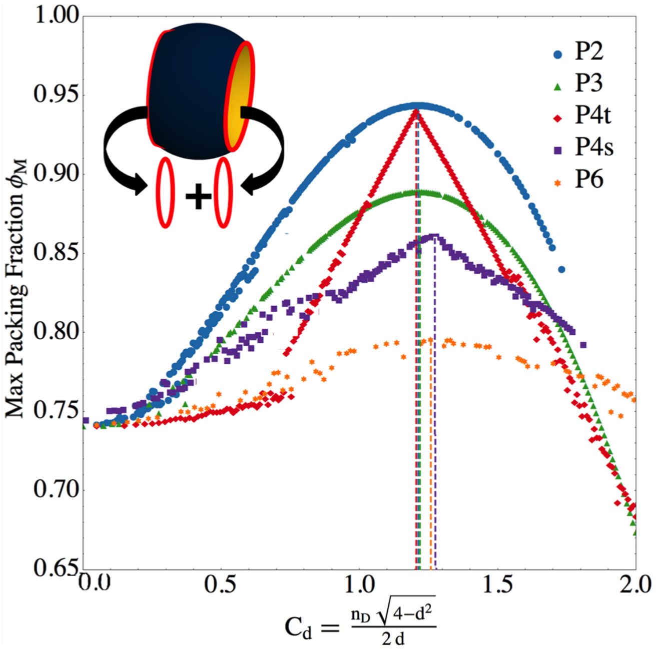

FIG. 4. Packing fraction ϕ vs the total dimple circumference-depth ratio C_d. The packing fraction reaches a critical maximum at $C_d^* = 1.234 \pm 0.060$.

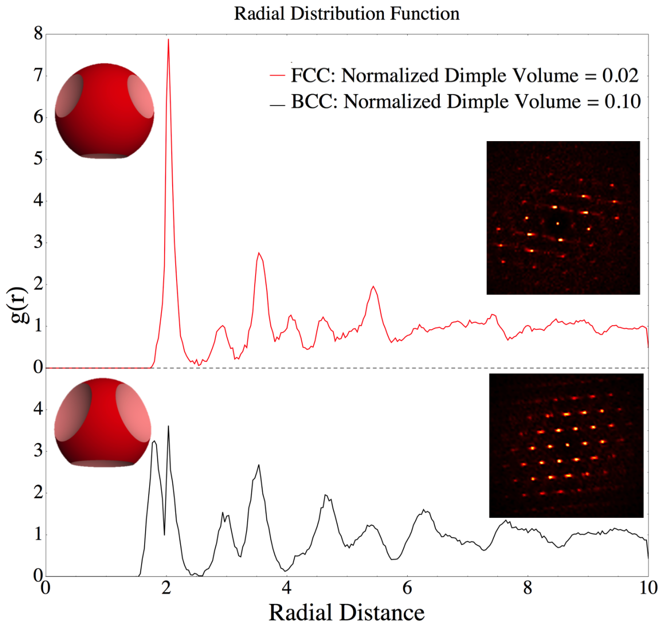

FIG. 5. The radial distribution function of tetrahedrally tetravalent particles (P4t) at infinitesimally small dimple volume (above) and small dimple volume (below). We report a transition from a face-centered cubic to a body-centered cubic crystal structure as volume of the dimple increases.

B. Self-Assembly

We also performed MC simulations at finite pressures to study assembly behavior away from the dense packing limit.

1. *Symmetry Independent Behavior near $f = 0$: Hard to Soft Transition*

In all cases, at $f = 0$ we observe the assembly of FCC lattices as we would expect for hard spheres. In all cases, as dimpling increases from $f = 0$ we observe a crossover from FCC to sheared BCT structures. The onset of the BCT structure occurs almost instantaneously as a result of continuous shearing from FCC into BCC structures.[42] The FCC-BCT transition is followed by a transition from BCT to BCC at dimple volume $v_d \sim 0.03$, which can, again, occur through simple shearing of the lattice.[42] The self-assembly of BCC structures from nearly spherical hard particles has been observed previously (see, e.g., [11, 37]). Here, by means of the radial distribution function, $g(r)$, (Fig. 5 shows an example for P4t particles) we see that in the BCC phase, neighboring particles penetrate into the dimples, but potential of mean force and torque (PMFT) calculations (Fig. 7a,c,e and Fig. 8a,c) show that, overall, the distribution of nearest neighbors remains relatively isotropic despite the presence of dimples. Other work [28, 43] has shown that soft spheres assemble BCC and other non-close packed lattices. In light of this prior work, our radial distribution function and PMFT results suggest that the BCC phases we observe here for nearly spherical particles, as well as those observed elsewhere (e.g. [11, 37]), arise because nearly spherical hard particles behave effectively as soft spheres, regardless of their symmetry.

2. *Symmetry Dependent Behavior at Large Dimpling*

Above a critical value $f \geq f^*_{SA}$ for each family, the phase behavior is dependent on the arrangement of dimples, as shown in Fig. 6 (for futher details, see appendix Figs. 18-22). P2 particles continue to self-assemble a BCC lattice, but the lattice takes on a parquet form in which particle orientations are ordered (see section III B 3). For P3 and P4t we do not observe spontaneous assembly of an ordered structure from a homogeneous fluid at any density on the time scale of our simulations. For P3, we find the expected triangular lattice is stable against melting to a packing fraction of 0.35 at dimpling amounts greater than 0.45. For P4t, if seeded, particles assemble a diamond lattice as found previously for tetrahedrally patterned enthalpically patchy particles [40], but unlike truncated tetrahedra [36] or tetrahedrally facetted spheres [11], which assemble without seeding. The diamond lattice does not melt down to a packing fraction of 0.26 at dimpling amounts greater than 0.60. P4s particles self-assemble a cubic lattice with rotational parquet symmetry. P6 particles self-assemble a simple cubic lattice. In all cases we observe that the crossover from BCC coincides with an emergent valence, or angular specificity, in the effective interactions between neighboring particles, on the order of a few $k_B T$ (see section III B 3), as has been observed for convex particles [5].

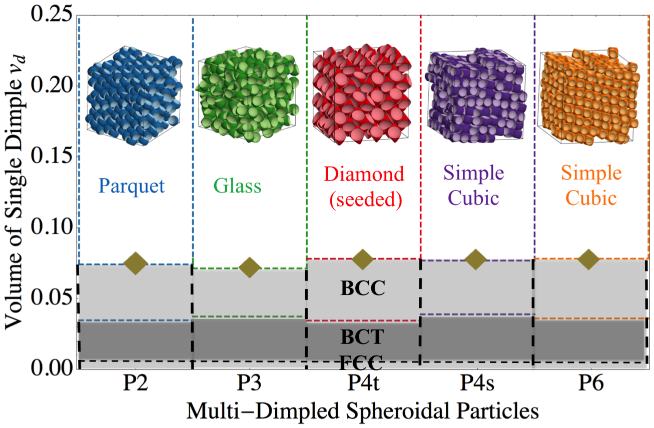

FIG. 6. Self-assembled crystals for different multi-dimpled spheroidal particles vs volume of individual dimples in particles. We find that critical volume of an individual dimple determines the spherical ($v_d \leq 0.07$) or non-spherical self-assembly of these particles. We also observe that hard spheres ($v_d = 0$) assemble into the FCC lattice. With the introduction of an infinitesimally small dimple, the sheared body-centered tetragonal structure is found. Above $v_d \geq 0.03$, we find that all particles assemble into the BCC lattice.Error bars are within the size of the gold markers.

3. *Potential of Mean Force and Torque*

The PMFT is a measure of the effective directional entropic forces (DEFs) that emerge for a pair of crowded particles [5]. The PMFT (Figs. 7, 8) shows how the local particle environment of multi-dimpled lock-and-key colloids differs in different bulk structures. We computed the PMFT at the lowest density where the crystal structure is formed, around a constant volume with a single particle placed at the center using methods introduced in our previous works [5, 11]. In the case of P3 and P4t particles, where no crystal structures are formed, we use the lowest stable density of the crystal structure obtained from melting studies of the densest packing structure. Figs. 7, 8 show isosurfaces of the PMFT in three dimensions plotted with VisIT [44]. In both columns, the PMFT is computed on the same constant volume. Below the critical dimpling amount f^*_{SA}, we observe a nearly isotropic effective entropic potential around the particle. At higher dimpling amounts, the dimples behave as an entropic patch [11] that results in a preferred directionality between pairs of crowded particles, similarly to what was observed previously for facetted spheres [5, 11].

For large dimples, the PMFT (Figs. 7b,d,f and 7b,d) show that a particle A adjacent to a dimpled particle B will coordinate at a dimple of particle B. This is similar to what has been observed previously for facetted spheres and polyhedra [5, 11]. However, in contrast to what has been observed previously for other shapes, depending on the structure, particle A will either preferentially align its convex region with the dimple of particle B, or will align its dimple with the dimple of particle B. This is a new feature that arises from the particle concavity. However, even in the case where both patches on neighboring particles align, the behavior differs from what has been observed previously. In the diamond crystal structure obtained from tetrahedrally tetravalent (P4t) particles, the dimples align facing each other, similarly to what has been observed previously [5, 11]. However, because of the concave nature of the entropic patches, there is considerable empty volume between the particles, resulting in stability at lower packing fraction of $\phi = 0.32$ than is evident from the structure, and what has been observed for convex particles [11, 36].

4. *Crossover in Self-Assembly from Symmetry Independent to Symmetry Dependent Behavior*

As in dense packing, with increasing dimple size, in each family we observe a change in system behavior. As we noted above, in all cases below some f^*_{SA}, we observed the self-assembly of BCC phases. Above f^*_{SA}, we observed phase behavior that depended on particle symmetry. The fact that in all cases we observed a loss of rotational entropy (captured in the PMFT results in Figs. 7, 8) driven by changing the particle geometry, suggests that there may be a common underlying geometric origin of this change in behavior. Depending on particle symmetry f^*_{SA} varied between 0.42 and 0.70 (66.6%), which suggests that, as in dense packing, f is not a good parameter for characterizing the origin of the crossover in bulk behavior. Instead, we found that the volume of an individual dimple on a multi-dimpled particle showed relatively small variation ($0.0714 \leq v_d \leq 0.0783$, or $\Delta v_d / v_d \approx 10\%$) at the crossover in bulk behavior across different particle symmetries.

We found that the change in bulk behavior coincides with the binding of particles at dimples, and that this coincides with an approximately constant volume of individual dimples. To understand why this might be the case, we note that Ref. [5] argued that the phase behavior of several systems of convex particles was driven by local packing considerations, which in example systems could be reduced to the consideration of simple, pairwise packing. Our results suggest the argument advanced in Ref. [5], i.e. that pairwise packing considerations are sufficient to understand the phase behavior of certain convex particles, extends to multi-dimpled sheres. We hypothesize why this is the case by considering what happens when a particle A binds entropically at a dimple of particle B. When particle A binds at the dimple of particle B, particle B loses rotational entropy on the order of $k_B \ln \Omega$ (where Ω is the number of distinct particle orientations[1]). This entropy loss is compensated by a gain in entropy for the rest of the system. It was argued in Ref. [5] that this should be determined by the stress tensor, which we can estimate as typically on the order of $k_B T / v_p$ where v_p is the particle volume. This suggests that the additional entropy gained by the system is on the order of $k_B v_d / v_p$, where, as particle pairs bind, we assume that the rest of the system gains free volume proportional to the dimple volume. There are key differences between systems: the pressure at the onset of ordering, the number of non-degenerate

---

[1] In technical terms, Ω is given by the volume of the relevant rotation group.

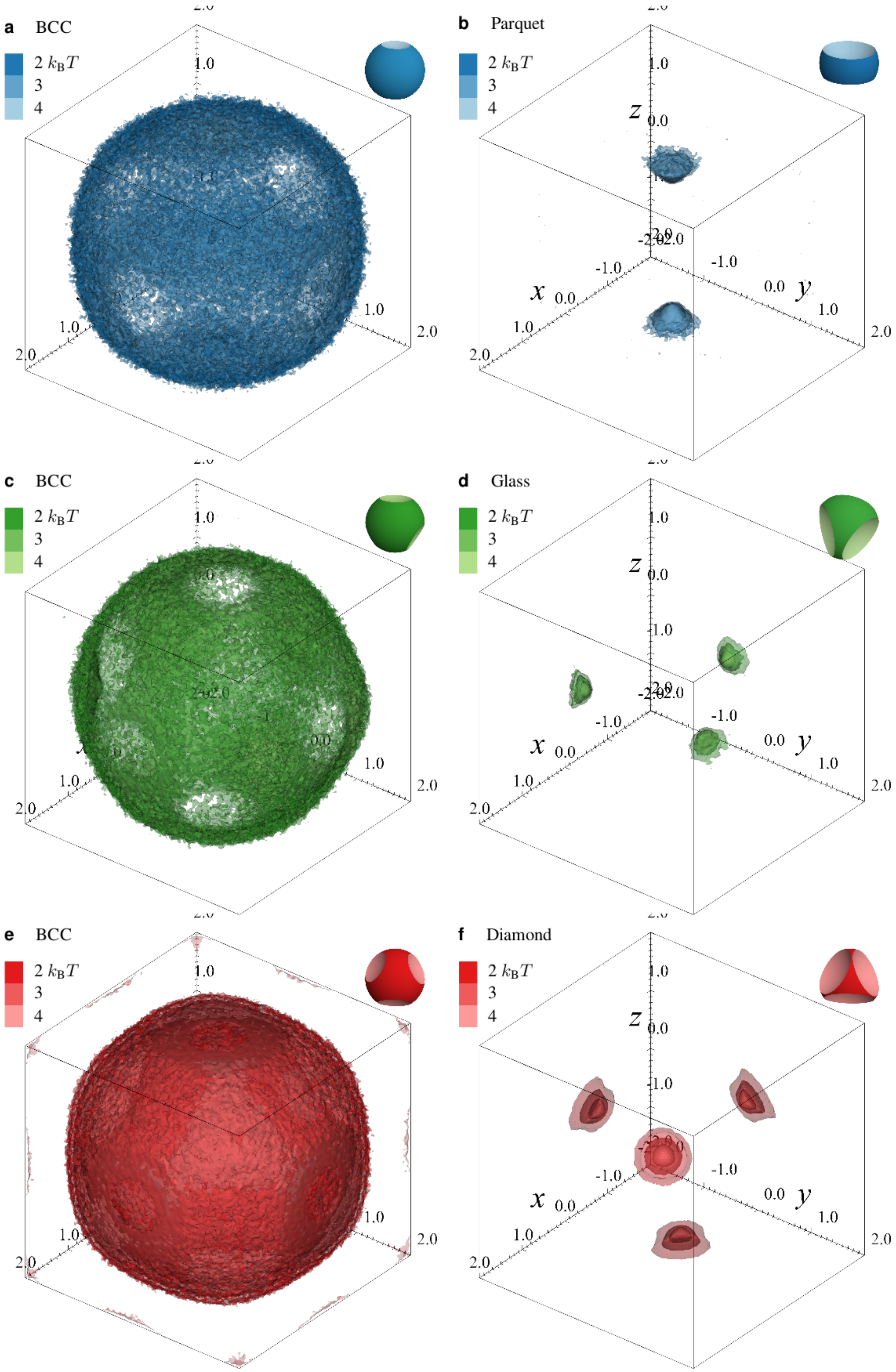

FIG. 7. Potential of mean force and torque (PMFT) calculations [5] show that below the critical dimpling amount f^*_{SA} (left) an isotropic potential exists. At higher dimpling amount (right), an attractive free energy well is presented in the volume of the dimple, giving rise to different crystal structures. (a, b) Bivalent particle showing (a) BCC and (b) parquet potentials. (c, d) Trivalent particle showing (c) BCC and (d) triangular sheet potentials. (e, f) Tetrahedrally tetravalent particle showing (e) BCC and (f) tetragonal diamond potentials.

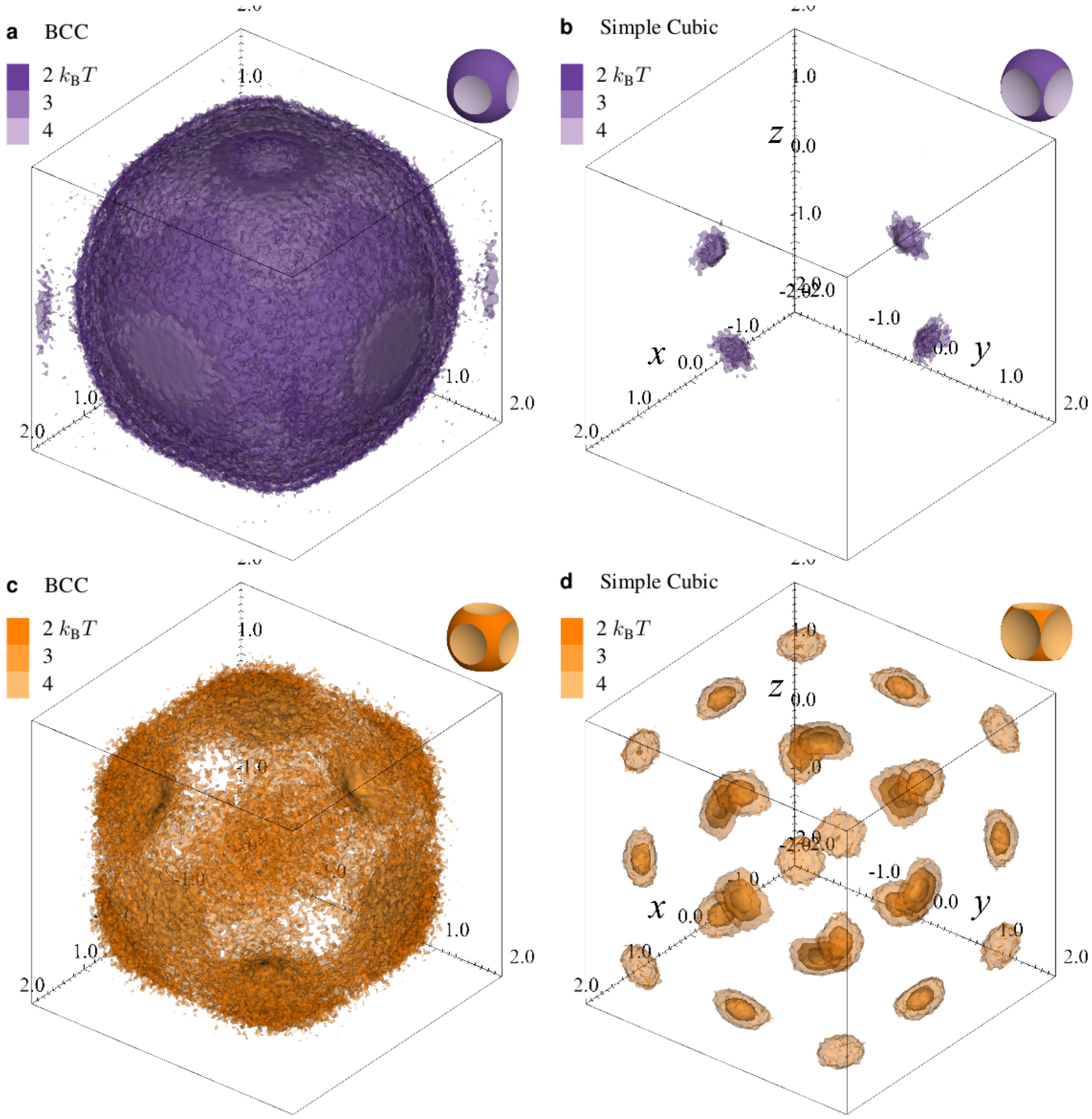

FIG. 8. Potential of mean force and torque (PMFT) calculations [5] show that below the critical dimpling amount f^*_{SA} (left) an isotropic potential exists. (a, b) Square Tetravalent particle showing (a) BCC and (b) simple cubic potentials. (c, d) Hexavalent particle showing (c) BCC and (d) simple cubic potentials. As the lattice vector of the cubic lattice formed is small in this case, we see second and third neighbor peaks in the cubic potential.

rotations (which is determined by the discrete symmetry of the particle), and the orientation of particles coordinated at dimples, it would be surprising to find perfect collapse for any geometric masure of ordering. Nevertheless, we find the variation in critical dimple volume is small.

We expect the result of dimple volume as the controlling feature for anisotropic assembly is specific to multi-dimpled lock-and-key colloids, and we do not expect this to be a phenomenon that generalizes to all shapes, e.g. to colloidal ellipsoids. Indeed prior work on facetted spheres suggested there that facet edges were important, but that was based on fewer examples than the present work [11]. However, what we have found is that the suggestion that the phase behavior of anisotropic colloids is controlled by pairwise effective interactions, as argued in Ref. [5], extends beyond the convex particles studied in [5], and suggests that the argument advanced in that work may be universal, even if the quantitative details of how it plays out for particles of different types is not.

IV. CONCLUSION

We found a structural crossover in packing that corresponds to a quantity that depends on *all* features of a particle shape, and one for the local ordering in assembly that depends on *in-*

dividual particle features. This finding is interesting in light of several studies showing discrepancies between the packing and assembly behavior of hard particles (e.g. [34, 36, 37, 45]). Recent work [5] has argued that the discrepancies between packing and assembly arise because assembly is driven by directional entropic forces that arise from balancing shape entropy, which in turn drives *local packing* whereas packing at infinite pressure is a global phenomenon in which entropy is irrelevant. Our finding, that the local ordering at low pressures where we observe assembly (to within 10%) controlled the geometry of individual particle features, whereas packing behavior is controlled (also to within 10%) by the geometry of all particle features, further supports the argument advanced in [5].

Interestingly, multi-dimpled particles self-assemble porous crystal structures at packing fractions of $40-50\%$ (and under certain conditions can remain at least metastable to much lower packing fractions), lower than that observed in convex systems (typically $\geq 50\%$ [11, 36, 37, 45, 46]). It has been proposed recently that entropy can stabilize open lattices in systems with both enthalpic and entropic contributions to the free energy [47]. Here, we found that entropy alone can stabilize porous structures. Intuition might suggest that the absence of strong enthalpic interactions in the present system may also result in fewer kinetic traps, and in several cases we found robust bulk 3D assembly. However, the kinetics of lock-and-key colloids are subtle: it has been shown that in the presence of depletants single-dimpled particles first make convex-to-convex contact before particles rearrange into convex-to-concave contact [26]. The existence of this complex kinetic pathway may explain why we did not observe the spontaneous global ordering of P3 or P4t particles here, despite those particles having DEFs in the range that causes other systems to self-assemble. Despite these exceptions, porous structures of the type we report here find applications in advanced catalysis and medical diagnosis [48]. The application of recently developed techniques for optimizing shapes for structures [12] to multi-dimpled particles might be useful for producing shapes that are less likely to get kinetically trapped.

Finally, we have described a set of systems that exhibit complex emergent, entropy-driven phase behavior that can be traced to a microscopic quantities that are approximately invariant under changes of particle symmetry. Because emergent behaviors are inherently difficult to ascribe to microscopic system details, we believe this example in experimentally realizable systems of colloids [19, 24] will provide a useful experimental setting for manipulating emergent behavior.

ACKNOWLEDGMENTS

We thank J. Crocker, M. Engel, and O. Gang for helpful discussions, and A. Karas for help with PMFT visualization. The U.S. Army Research Office under Grant Award No. W911NF-10-1-0518 and the DOD/ASD(R&E) under Award No. N00244-09-1-0062 supported the assembly work. The Biomolecular Materials Program of the Materials Engineering and Science Division of Basic Energy Sciences at the U.S. Department of Energy under Grant No. DE-FG02-02ER46000 supported the packing studies and PMFT calculations. ERC acknowledges NSF MSPRF grant DMS-1204686.

Appendix A: Geometric Characteristics of Multi-Dimpled Particles

We calculate geometric characteristics of the particles at various dimpling amounts, as shown in Figure 9.

1. Dimple Volume

The volume of a single dimple, v_d, is the union of the volume of the two intersecting spherical caps that form the dimple. The volume of spherical cap of radius R and height h is given by

$$V(R,h) = \tfrac{1}{3}\pi h^2(3R-h)\,.$$

For a single dimple formed at the intersection of central and valence spheres of radii R_+, R_-, its volume is given by

$$\begin{aligned} v_d = {} & \tfrac{\pi}{12d}(R_+ + R_- - d)^2 \times \\ & (d^2 + 2dR_+ + 2dR_- + 6R_+R_- - 3R_+^2 - 3R_-^2) \end{aligned} \tag{A1}$$

. For $R_+ = R_- = 1$,

$$v_d = \tfrac{\pi}{12}(d+4)(2-d)^2\,. \tag{A2}$$

where d is the distance between the centers of the central sphere and the valence sphere. The volume of the remaining particle v_{sp} is given by

$$v_{sp} = v_{PS} - (n_D \times v_d)\,. \tag{A3}$$

where v_{PS} is the volume of the original central sphere, v_d is the volume of a single dimple and n_D is the number of dimples in the particle. This gives

$$v_{sp} = \tfrac{4}{3}\pi R_+^3 - n_D \times \tfrac{\pi}{12}(d+4)(2-d)^2\,. \tag{A4}$$

We normalize the total dimple volume for a particle by

$$V_d = \frac{n_D \times v_d}{v_{sp}}\,. \tag{A5}$$

For normalized single dimple volume, we set $n_D = 1$.

2. Dimple Surface Area

Similar to the volume of the dimples, we calculate the surface area of a single dimple and normalize the total surface area of the dimples by the surface area of the particle. The surface area of a single dimple s_d is calculated as the surface area of a spherical cap formed between the central and valence

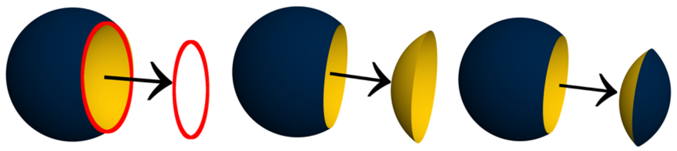

(a) Circumference (b) Surface Area (c) Volume

FIG. 9. The different shape features of multi-dimpled spheres considered in this study.

spheres. For spheres of radii R_+, R_-, the surface area is given by

$$s_d = \frac{\pi R_-}{d}(R_+ - R_- + d)(R_+ + R_- - d)\,. \tag{A6}$$

For $R_+ = R_- = 1$,

$$s_d = \pi(2-d)\,. \tag{A7}$$

The surface area of the particle, s_{sp}, is given by

$$s_{sp} = s_{PS} - (n_D \times s_d)\,. \tag{A8}$$

where s_{PS} is the surface area of the original central sphere. This gives

$$s_{sp} = 4\pi R_+^2 - n_D \times \pi(2-d)\,. \tag{A9}$$

The self-assembled non-spherical crystal structure is rather dependent on the number and arrangement of dimples in the particle. We normalize the total dimple surface area S_d for a particle as

$$S_d = \frac{n_D \times s_d}{s_{sp}}\,. \tag{A10}$$

3. Dimple Circumference

Similarly, the circumference of the dimples c_d is calculated from the radius of the circle of intersection between the central and valence spheres. For spheres of radii R_+, R_-, the circumference is given by

$$c_d = \frac{\pi}{d}\sqrt{(-R_+ + R_- + d)(R_+ - R_- + d)}\times \sqrt{(R_+ + R_+ - d)(R_+ + R_- + d)} \tag{A11}$$

. For $R_+ = R_- = 1$,

$$c_d = \pi\sqrt{4-d^2}\,. \tag{A12}$$

This circumference is normalized by the distance between the central and valence spheres. To reduce the numerical ratio, we use a weight 2π and call this normalization factor c_{sp}. This factor is given by

$$c_{sp} = 2\pi d\,. \tag{A13}$$

The total circumference of the dimples C_d is thus normalized by the circumference of a circle describing the distance between the parent and valence sphere in the particle.

$$C_d = \frac{n_D \times c_d}{c_{sp}}\,. \tag{A14}$$

Appendix B: Critical Dimpling Amount

TABLE II. Crossover Values for Putative Densest Packings and Thermodynamic Assemblies

Particle	f_{DP}^*	C_d	f_{SA}^*	v_d
P2	0.73	1.21	0.42	0.0742
P3	0.53	1.22	0.48	0.0714
P4t	0.35	1.20	0.53	0.0782
P4s	0.66	1.32	0.73	0.0769
P6	0.30	1.26	0.70	0.0783

The critical dimpling amount for the putative densest packing f_{DP}^* and self-assembly f_{SA}^* of each type of multi-dimpled particle is the crossover point in the corresponding particle behavior. At these crossover values, different geometric characteristics of each particle type have been computed as shown in Table II.

To understand the packing of multi-dimpled spheroidal particles, we determine the primary feature in the shape of these particles that affects their behavior. We investigate the value of f_{DP}^* compared to the total volume V_d, surface area S_d and circumference C_d of all dimples on a single particle as d is varied. We normalize each of these three parameters. The volume and surface area are normalized by the remaining respective quantity in a single particle, while the circumference is normalized by the circumference of a circle with radius equal to the distance between the central and valence spheres, a linear function of the depth of the dimple. We compute the total normalized dimple volume, surface area and circumference to depth ratio in each family of particle at f_{DP}^*. We find that the total circumference to depth ratio C_d of the dimples is 1.23 ± 0.06 at f_{DP}^* across all five particle families; see Fig. 4. In contrast, no dimple volume or surface area showed no similar collapse.

We also observed that in self-assembly, all particle types undergo a structural transition from BCC in which particles have nearly isotropic pairwise interactions, into a phases where particle symmetry is important. To quantify when the concave features are sufficient to induce a change in the preferred structure, we compare particle shape characteristics at the critical dimpling amount for self assembly f_{SA}^*. We find that, across particle types, v_d shows little variation at f_{SA}^*, which suggests that *the volume of individual dimples controls assembly behavior, independent of particle type.*

TABLE III. Geometric and Numerical Calculations of Particle Interlocking

Particle	Description	f_{DP}^*	$f_{DP}^\dagger$	d^2
P2	Bivalent	0.73	0.86	2.0
P3	Trivalent	0.53	0.70	2.14

Appendix C: Analytic Calculations of Packings

To verify the putative densest packing predicted computationally via MC simulations for the particles studied, analytic calculations of the packings of these particles were performed. In Figures 10 - 14, we plot analytic calculations of the packing curve and numerically predicted packings for one and two particles of all particle types. We show that our numerical calculations match the analytic findings to within 0.001% when $f \geq 0.10$. Additionally, we perform numerical and analytic packing calculations for single dimpled particles (see Figure 15). We find that single dimpled particles do not follow the pattern shown by other particles in this study due to the lack of discrete symmetry in their shape.

We further numerically calculate maximum packing densities of all particle types with up to eight particles. However, due to the complexity of the analytic packing problem for number of particles $n \geq 3$, we do analytic calculations only for (some) one- and two-particle packings ($n = 1, 2$) for different particle types. If solvable, these analytic curves and intersection equations are shown in Figures 15 - 17. For these results it is useful to work in terms of a linearly shifted parameter $\mathcal{F} = 0.5d$, where d is the distance parameter, rather than the dimpling parameter f we use in the main text. We denote the volume of a particle by U, the volume of a unit cell of the lattice by V, the packing fraction by φ, and different packing regions by Υ. We denote the vectors describing a unit cell of the packing as α, β, and γ, and the volume is given by the standard formula $V = \alpha \cdot (\beta \times \gamma)$. Images are colored so that the color on the left hand side of the image matches the color used for the particle in the rest of the text, and then proceeds through the visual spectrum over the range of geometrically allowed particle parameters starting toward the red end of the spectrum for single particle packings, and the blue end of the spectrum for two particle packings.

The relationship between the thickness parameter $\mathcal{F}$ and dimpling parameter f for each particle type is included in the bottom left side of the graph. Analytic calculations of the dimensions of the packing box are shown in the graph. The analytic packing density curve is drawn as a line in these figures against the thickness parameter $\mathcal{F}$, in regions where it can be calculated. In order to compare with putative density calculations, these lines are superimposed on markers denoting numerical calculations. Various regions in these analytic packing curves are explicitly marked through vertical lines at different values of $\mathcal{F}$, the thickness parameter. In regions where the analytic curves can be calculated, we find that they match our numerical calculations, with an error less than 0.001% when $f \geq 0.10$. We include the single dimpled particle P1, since the same lattice Υ_1 is shared between particles P1 and P2. Similarly, the same lattice Υ_2 is shared among particles P2, P4s and P6.

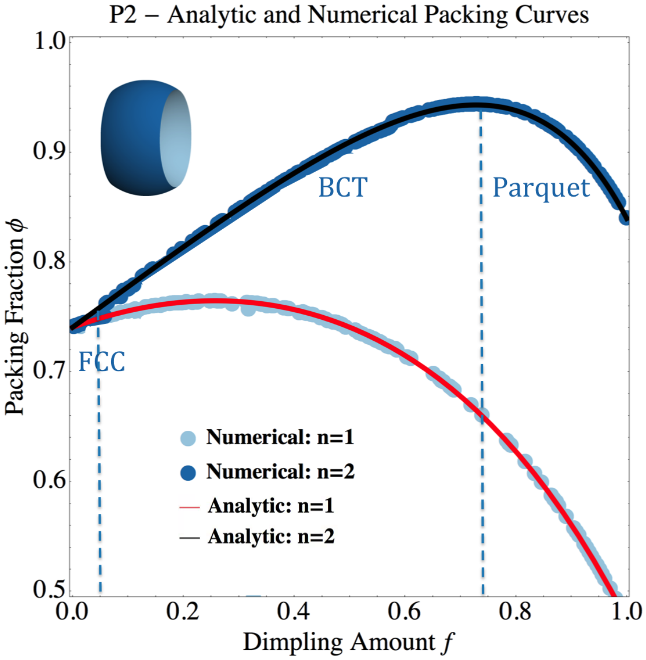

FIG. 10. Analytic and numerical packing curves showing a perfect fit for bivalent particle (P2) for one and two particles in a box. Analytic packing curve for one particle is shown in red, two particles in black. The dark markers denote numerical densest packing calculations for two particles in a box, and light for one particle. Blue dashed lines show the different packing regions found in numerical calculations.

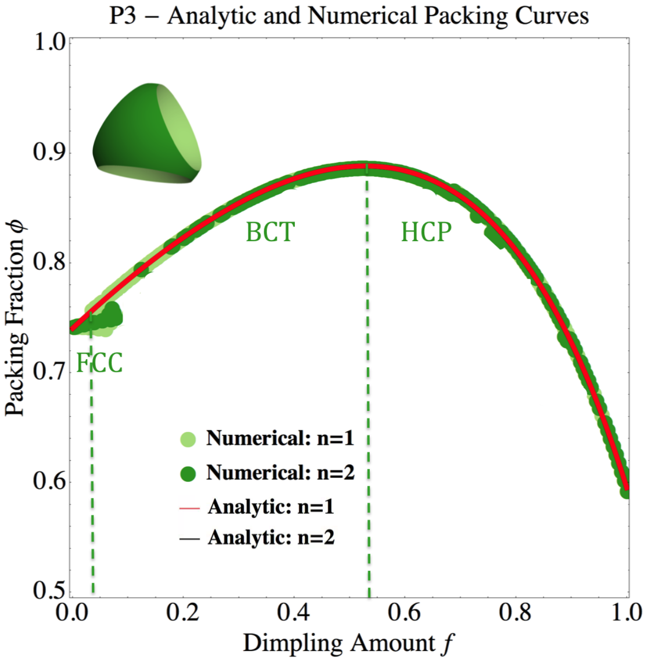

FIG. 11. Analytic and numerical packing curves showing a perfect fit for trivalent particle (P3) for one and two particles in a box. The curves overlap as one and two particles pack in the same manner. Green dashed lines show the different packing regions found in numerical calculations.

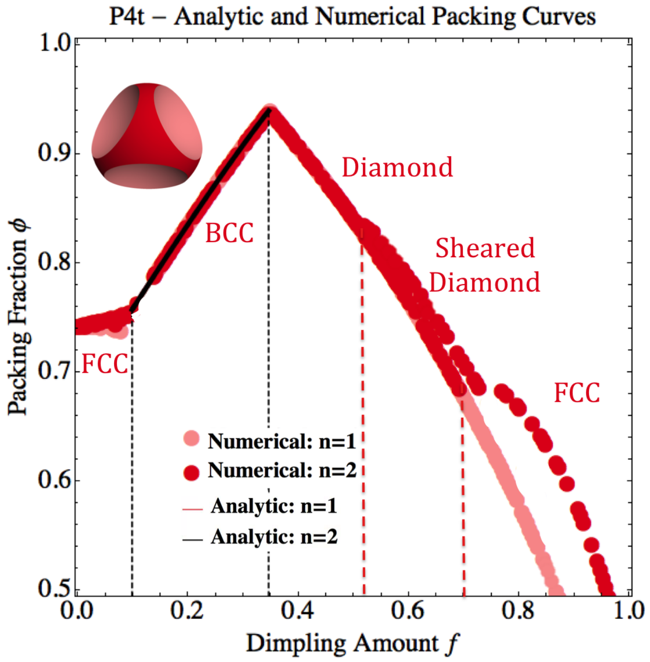

FIG. 12. Analytic and numerical packing curves showing a perfect fit in a single region between black dashed lines for tetrahedral tetravalent particle (P4t) of one and two particles in a box. Analytic packing equations could not be calculated at all dimpling amounts by analytic means. Red dashed lines show the different packing regions found in numerical calculations, in addition to those found in analytic calculations.

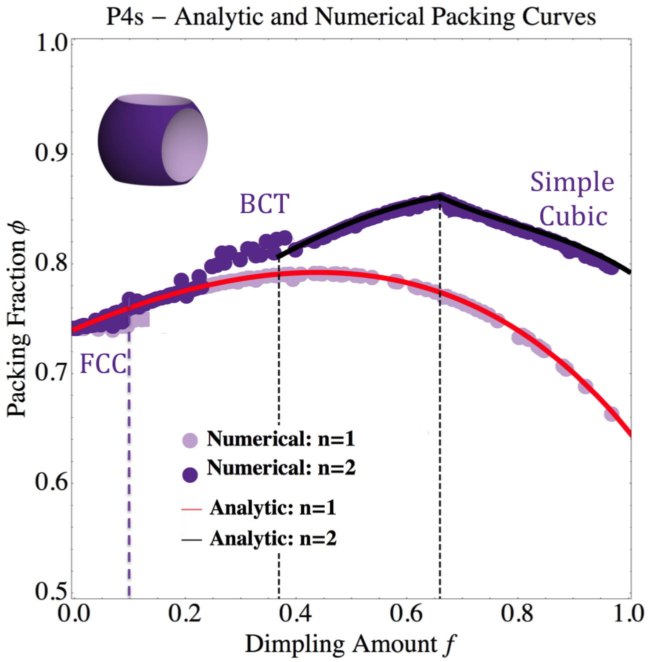

FIG. 13. Analytic and numerical packing curves of a square tetravalent particle (P4s) showing a perfect fit in the entire domain for one particle in a box and between black dashed lines in two regions for two particles in a box. Analytic packing curves could not be calculated at all dimpling amounts for two particles by analytic means. Magenta dashed lines show the different packing regions found in numerical calculations, in addition to those found in analytic calculations.

Appendix D: Self-Assembly

1. Transition Density

The particles studied in this work assemble at approximately the same conditions. For the sake of completeness, we show the transition density phase diagrams for thermodynamic self-assembly of each particle in Figures 18 – 22. In these plots, we also observe the reported behavior of a crossover in the assembly of particles beyond a constant critical volume of a single dimple in the top axis.

These crystal structures are formed by entropic interactions between the convex and concave regions of two adjacent particles. We find that the emergent valence is dependent on the geometry of the dimples (see section III B 3 for details). The number of directions for the alignment of the particles depends on the crystal lattice, for example, two in the parquet structure. It should also be noted that the particles have rotational symmetries, which align with the symmetry of the crystals and thus do not break the symmetry of the crystals. In the case of the tetrahedrally tetravalent particle, particles have two orientations in the diamond crystal structure formed.

The self-assembly of multi-dimpled spheres into crystal structures occurs at packing fractions of 40 – 50%, much lower than that observed in entropically driven assemblies of convex polyhedra, typically $> 50\%$. These assemblies are thus candidate structures for entropically assembled porous structures, and can find applications such as advanced catalysis. By designing porous structures using entropy alone, their assembly pathways have lesser kinetic traps than their enthalpic counterparts, giving rise to structures that can be easily assembled and reconfigured.

2. Dimpling Amount and Volume of a Dimple

As shown in Figures 18 – 22, the phase diagrams do not collapse at a constant dimpling amount f. However the volume of a single dimple is constant at the crossover across all phase diagrams. Here we include calculations that show the relationship between volume of a single dimple and the dimpling amount, in order to show that these two quantities are not linear functions of each other.

For bivalent particle, P2, with two dimples, we have:

$$\begin{aligned} f &= \frac{4-d^2}{4-1}\,, \\ d^2 &= 4-3f\,. \end{aligned} \tag{D1}$$

where, f is a linear mapping of d^2, the distance between the valence and central spheres.

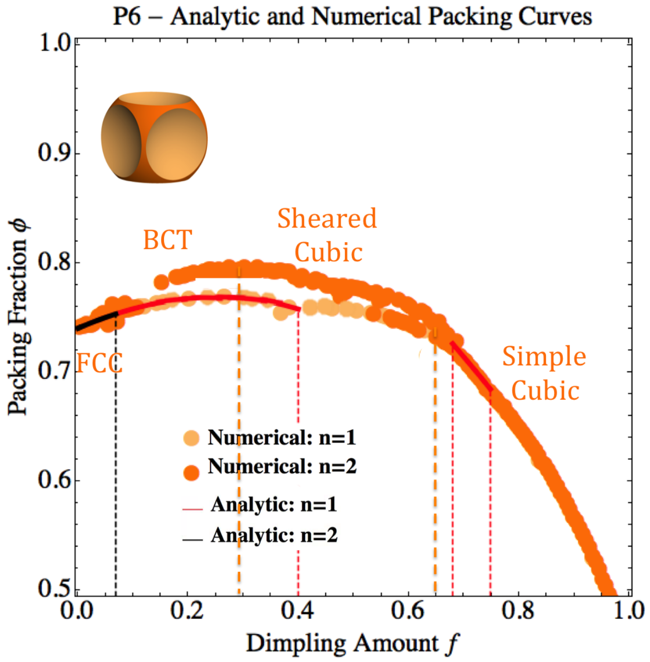

FIG. 14. Analytic and numerical packing curves of a hexavalent particle (P6) showing a perfect fit between red dashed lines in two regions for one particle in a box and between black dashed lines in one region for two particles in a box. Analytic packing curves could not be calculated at all dimpling amounts for two particles by analytic means. Orange dashed lines show the different packing regions found in numerical calculations, in addition to those found in analytic calculations.

Next, we have:

$$V_d = \frac{v_d}{v_{sp}} \, ,$$
$$V_d = \frac{(d+4)(2-d)^2}{8-(d+4)(2-d)^2} \, . \tag{D2}$$

where, V_d is the normalized single dimple volume, equivalent to the ratio of the volume of a single dimple to the volume of the remaining particle.

In a similar fashion, we understand that the relationship between the volume of a single dimple and the dimpling amount is different for each particle type and is a function of the dimple geometry in a particle.

[1] F. Cucker and S. Smale, IEEE Trans. Automat. Contr. **52**, 852 (2007)

[2] P. Aynajian, E. H. da Silva Neto, A. Gyenis, R. E. Baumbach, J. D. Thompson, Z. Fisk, E. D. Bauer, and A. Yazdani, Nature **486**, 201 (2012)

[3] P. Anderson, Science **177**, 393 (1972)

[4] R. D. Kamien, in *Soft Matter, Volume 3, Colloidal Order: Entropic and Surface Forces*, edited by G. Gompper and M. Schick (Wiley-VCH, Weinheim, 2007)

[5] G. van Anders, D. Klotsa, N. K. Ahmed, M. Engel, and S. C. Glotzer, Proc. Natl. Acad. Sci. **111**, E4812 (2014)

[6] F. A. Escobedo, Soft Matter **10**, 8388 (2014)

[7] A. B. Pawar and I. Kretzschmar, Macromol. Rapid Commun. **31**, 150 (2010)

[8] S. Sacanna and D. J. Pine, Curr. Opin. Colloid Interface Sci. **16**, 96 (2011)

[9] A. Shah, B. Schultz, W. Zhang, S. C. Glotzer, and M. J. Solomon, Nat. Mater. **14**, 117 (2014)

[10] V. Prasad, D. Semwogerere, and E. R. Weeks, J. Phys. Condens. Matter **19**, 113102 (2007)

[11] G. van Anders, N. K. Ahmed, R. Smith, M. Engel, and S. C. Glotzer, ACS Nano **8**, 931 (2014)

[12] G. van Anders, D. Klotsa, A. S. Karas, P. M. Dodd, and S. C. Glotzer, ACS Nano **9**, 9542 (2015), arXiv:1507.04960 [cond-mat.soft]

[13] S. Sacanna, W. T. M. Irvine, P. M. Chaikin, and D. J. Pine, Nature **464**, 575 (2010)

[14] G. Odriozola, F. Jiménez-Angeles, and M. Lozada-Cassou, J. Chem. Phys. **129**, 111101 (2008)

[15] M. Marechal, R. J. Kortschot, A. F. Demirörs, A. Imhof, and M. Dijkstra, Nano Lett. **10**, 1907 (2010)

[16] M. Marechal and M. Dijkstra, Phys. Rev. E **82**, 031405 (2010)

[17] G. Odriozola and M. Lozada-Cassou, Phys. Rev. Lett. **110**, 105701 (2013)

[18] D. J. Ashton, R. L. Jack, and N. B. Wilding, Soft Matter **9**, 9661 (2013)

[19] Y. Wang, Y. Wang, X. Zheng, G.-R. Yi, S. Sacanna, D. J. Pine, and M. Weck, J. Am. Chem. Soc. **136**, 6866 (2014)

[20] W. Wang, M.-J. Zhang, R. Xie, X.-J. Ju, C. Yang, C.-L. Mou, D. A. Weitz, and L.-Y. Chu, Angew. Chem. Int. Ed. **52**, 8084 (2013)

[21] S.-H. Kim, A. D. Hollingsworth, S.-J. Sacanna, Stefano and-Chang, G. Lee, D. J. Pine, and G.-R. Yi, Journal of the American Chemical Society **134**, 16115 (2012)

[22] S. Sacanna, M. Korpics, K. Rodriguez, L. Colon-Melendez, S.-H. Kim, D. J. Pine, and G.-R. Yi, Nat. Commun. **4**, 1688 (2013)

[23] S. J. Ivell, R. P. A. Dullens, S. Sacanna, and D. G. A. L. Aarts, Soft Matter **9**, 9361 (2013)

[24] A. Désert, C. Hubert, Z. Fu, L. Moulet, J. Majimel, P. Barboteau, A. Thill, M. Lansalot, E. Bourgeat-Lami, E. Duguet, and S. Ravaine, Angew. Chem. Int. Ed. Eng. , 1 (2013)

[25] S. Sacanna, W. T. M. Irvine, L. Rossi, and D. J. Pine, Soft Matter **7**, 1631 (2011)

[26] L. Colón-Meléndez, D. Beltrán-Villegas, G. van Anders, J. Liu,

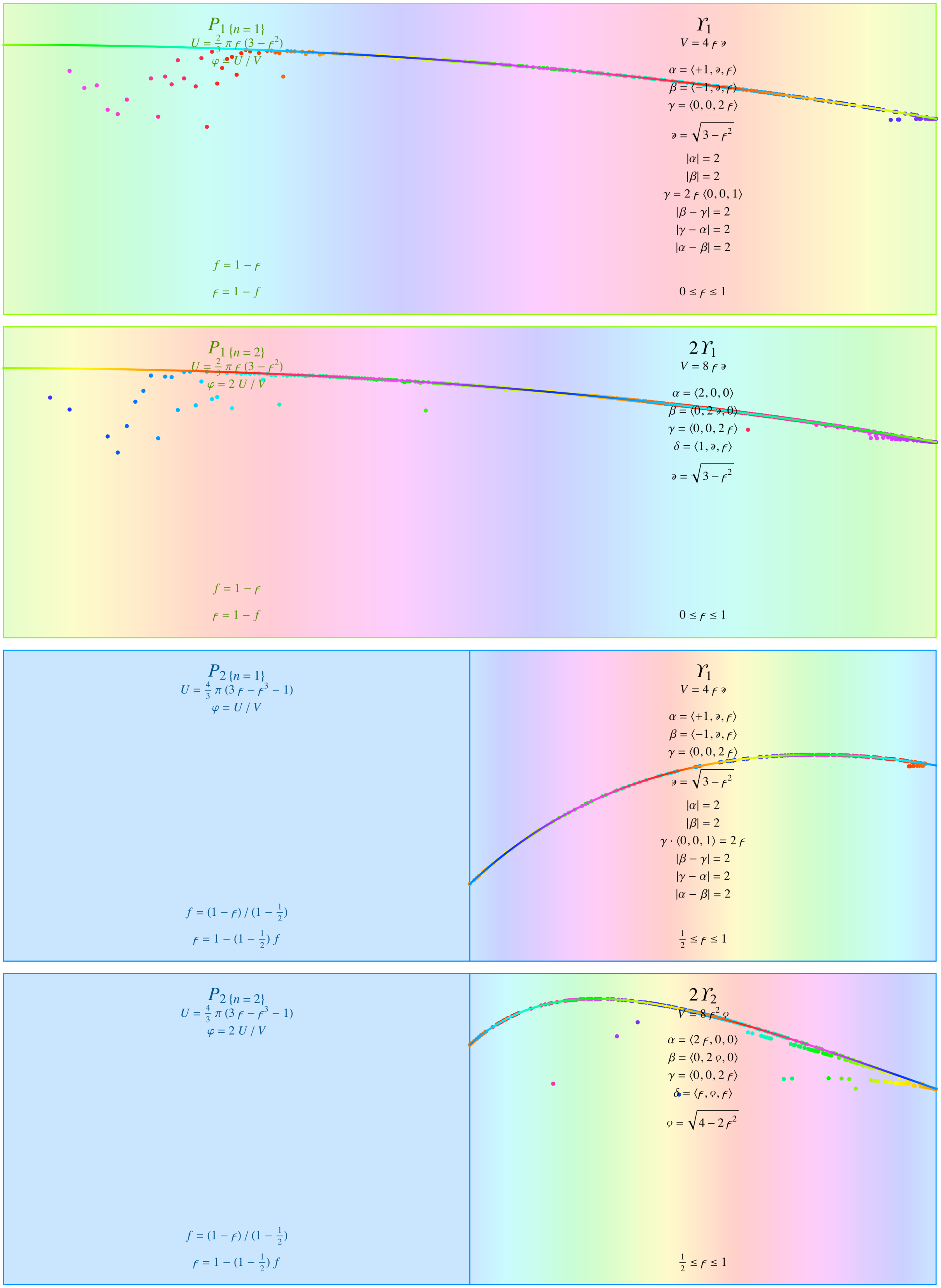

FIG. 15. Analytic packing density $\frac{3}{10} \leq \phi \leq 1$ and packing curves as a function of thickness parameter $0 \leq \digamma \leq 1$ (*right*) for single & double lattice packings of particles P1 & P2.

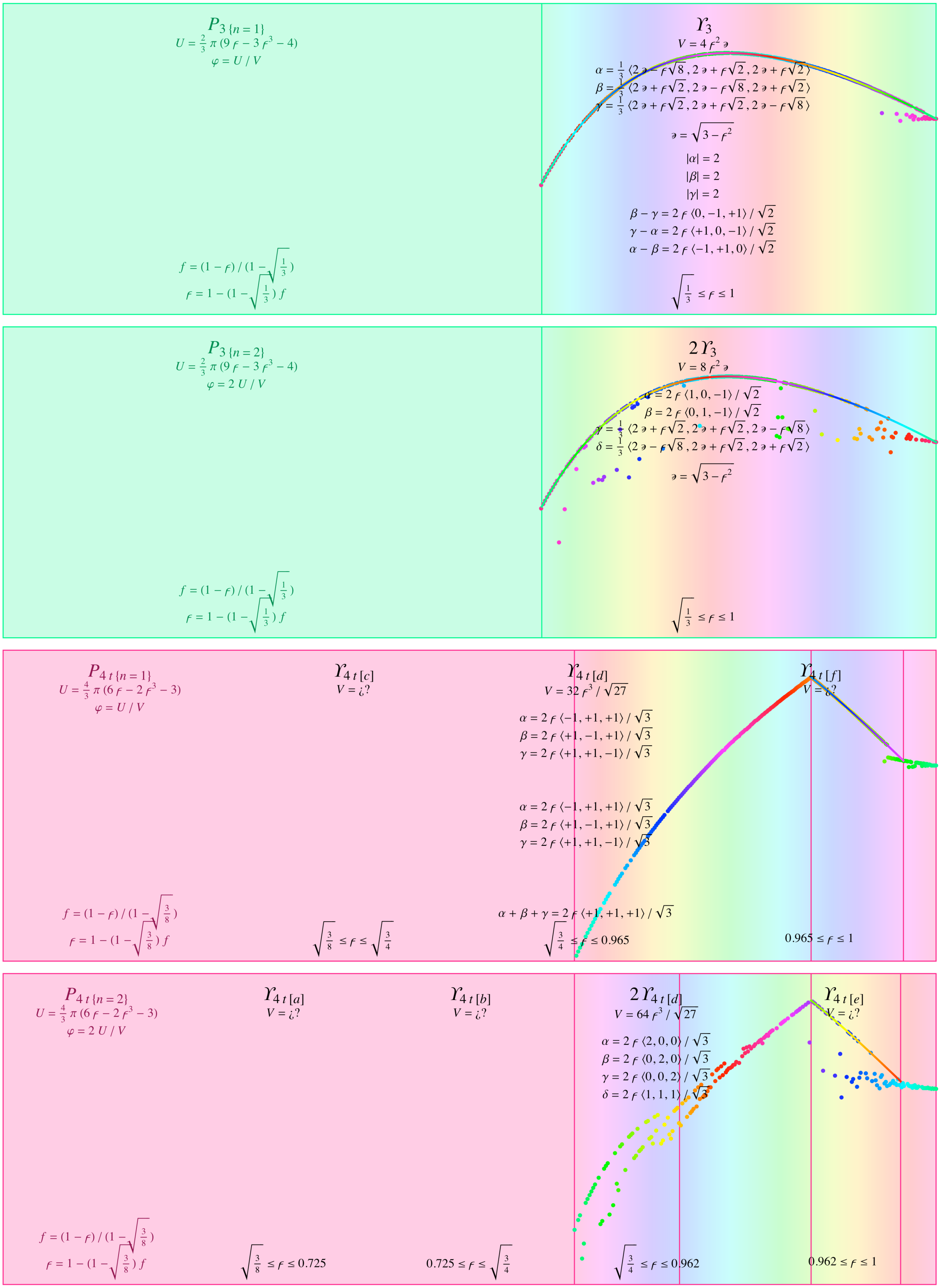

FIG. 16. Analytic packing density $\frac{3}{10} \le \phi \le 1$ and packing curves as a function of thickness parameter $0 \le \digamma \le 1$ (*right*) for single & double lattice packings of particles P3 & P4t.

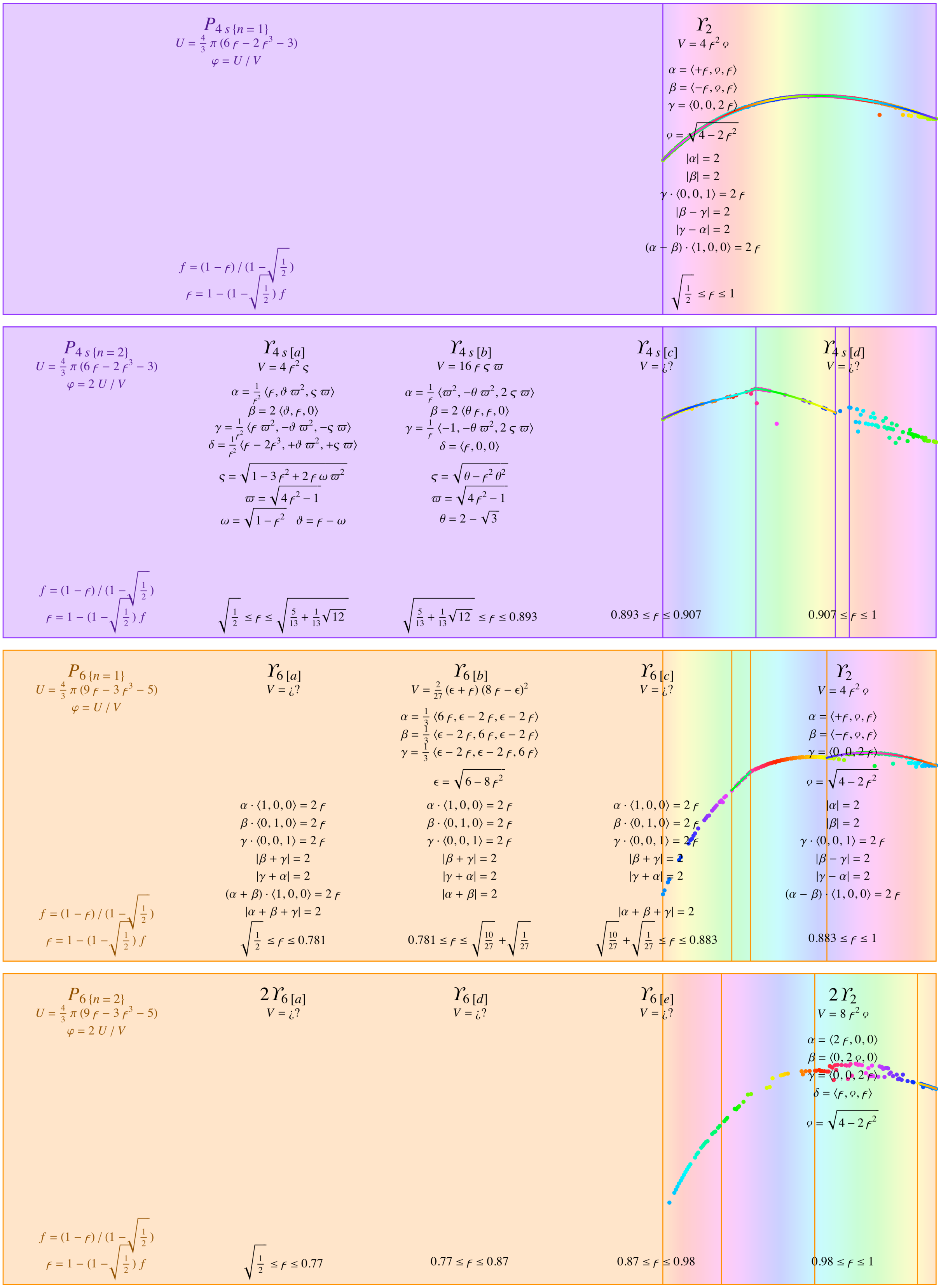

FIG. 17. Analytic packing density $\frac{3}{10} \le \phi \le 1$ and packing curves as a function of thickness parameter $0 \le \digamma \le 1$ (*right*) for single & double lattice packings of particles P4s & P6.

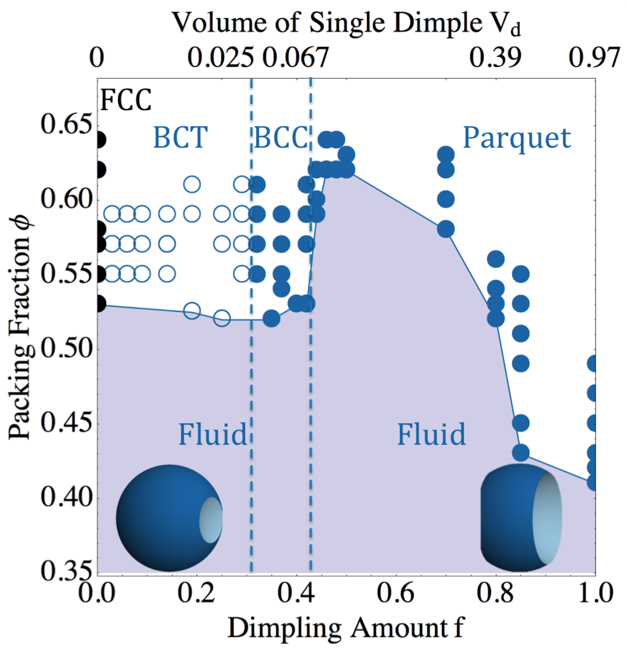

FIG. 18. Minimum packing fraction at which bivalent particles (P2) assemble crystal structures. The structures assembled vary with dimpling amount f, from FCC for hard sphere to BCT, BCC and a parquet structure. Blue dashed lines show the different structural regions found in our simulations.

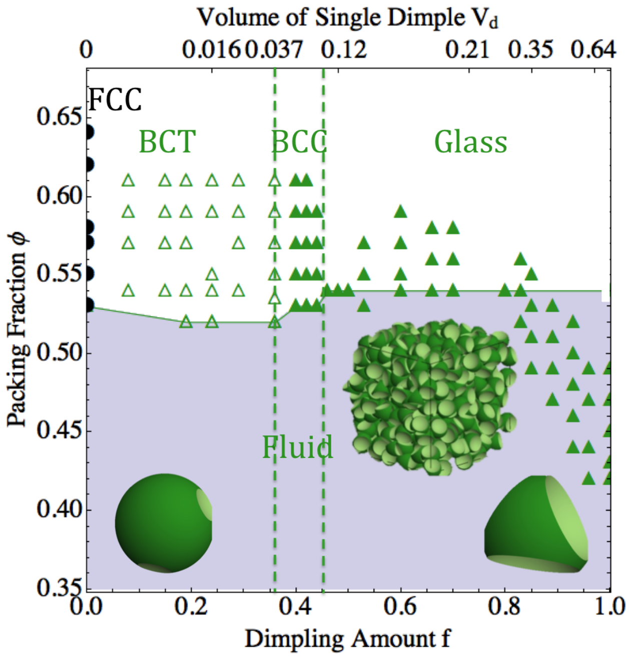

FIG. 19. Minimum packing fraction at which trivalent particles (P3) assemble crystal structures. The structures assembled vary with dimpling amount f, from FCC for hard sphere to BCT, BCC and then form glass. Green dashed lines show the different structural regions found in our simulations.

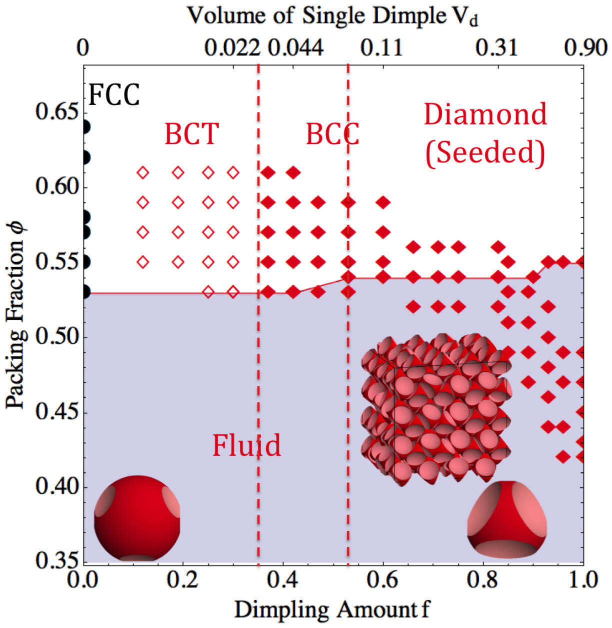

FIG. 20. Minimum packing fraction at which tetrahedral tetravalent particles (P4t) assemble crystal structures. The structures assembled vary with dimpling amount f, from FCC for hard sphere to BCT, BCC and diamond. Red dashed lines show the different structural regions found in our simulations.

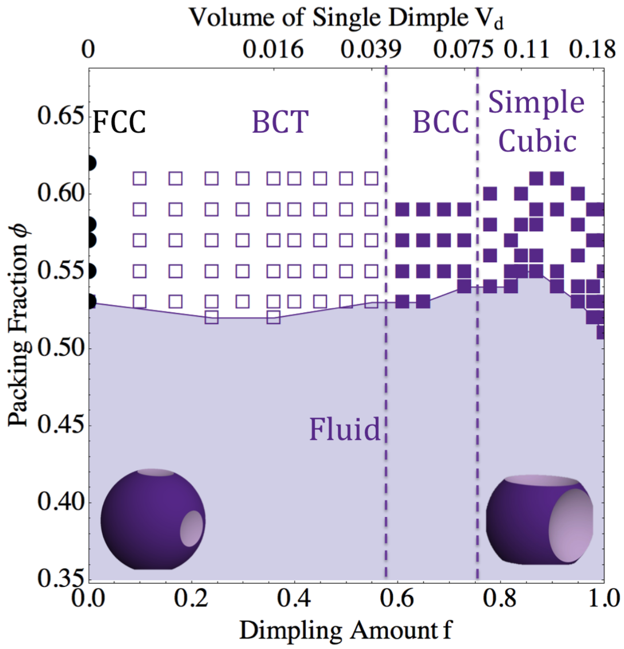

FIG. 21. Minimum packing fraction at which square tetravalent particles (P4s) assemble crystal structures. The structures assembled vary with dimpling amount f, from FCC for hard sphere to BCT, BCC and simple cubic. Purple dashed lines show the different structural regions found in our simulations.

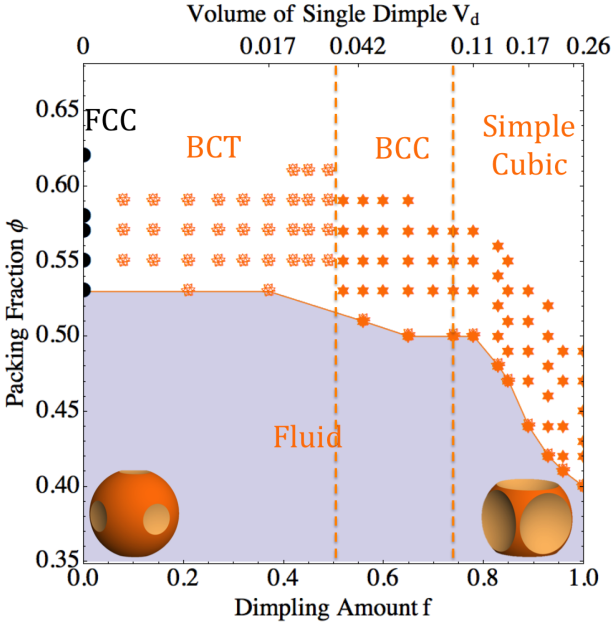

FIG. 22. Minimum packing fraction at which hexavalent particles (P6) assemble crystal structures. The structures assembled vary with dimpling amount f, from FCC for hard sphere to BCT, BCC and simple cubic. Yellow dashed lines show the different structural regions found in our simulations.

M. P. Spellings, S. Sacanna, D. J. Pine, S. C. Glotzer, R. G. Larson, and M. J. Solomon, J. Chem. Phys. **142**, 174909 (2015), 10.1063/1.4919299

[27] T. C. Hales, Ann. Math. Second Ser. **162**, 14 (2002), arXiv:0205209 [math]

[28] M. O. Robbins, K. Kremer, and G. S. Grest, J. Chem. Phys. **88**, 3286 (1988)

[29] E. Gilbert, D. Johnson, and S. Keerthi, IEEE J. Robotics and Automation **4**, 193 (1988)

[30] G. Cinacchi and J. S. van Duijneveldt, J. Phys. Chem. Lett. **1**, 787 (2010)

[31] G. Cinacchi, J. Chem. Phys. , 124908 (2013)

[32] M. He and P. Siders, J. Phys. Chem. **94**, 7280 (1990)

[33] E. R. Chen, preprint (2014)

[34] A. Haji-Akbari, M. Engel, A. S. Keys, X. Zheng, R. G. Petschek, P. Palffy-Muhoray, and S. C. Glotzer, Nature **462**, 773 (2009)

[35] E. R. Chen, M. Engel, and S. C. Glotzer, Discrete Comput. Geom. **44**, 253 (2010)

[36] P. F. Damasceno, M. Engel, and S. C. Glotzer, ACS Nano **6**, 609 (2012)

[37] P. F. Damasceno, M. Engel, and S. C. Glotzer, Science **337**, 453 (2012)

[38] D. Ortiz, K. L. Kohlstedt, T. D. Nguyen, and S. C. Glotzer, Soft Matter **10**, 3541 (2014)

[39] E. R. Chen, D. Klotsa, M. Engel, P. F. Damasceno, and S. C. Glotzer, Phys. Rev. X **4**, 011024 (2014)

[40] Z. Zhang, A. S. Keys, T. Chen, and S. C. Glotzer, Langmuir **21**, 11547 (2005)

[41] Y. Kallus and V. Elser, Phys. Rev. E **83**, 036703 (2011)

[42] R. A. Dunlap, Eur. J. Phys. Educ. **3**, 1 (2012)

[43] Y. Monovoukas and A. P. Gast, J. Colloid Interface Sci. **128**, 533 (1989)

[44] H. Childs, E. Brugger, B. Whitlock, J. Meredith, S. Ahern, D. Pugmire, K. Biagas, M. Miller, C. Harrison, G. H. Weber, H. Krishnan, T. Fogal, A. Sanderson, C. Garth, E. W. Bethel, D. Camp, O. Rübel, M. Durant, J. M. Favre, and P. Navrátil, in *High Performance Visualization–Enabling Extreme-Scale Scientific Insight* (2012) pp. 357–372

[45] U. Agarwal and F. A. Escobedo, Nat. Mater. **10**, 230 (2011)

[46] J. de Graaf, R. van Roij, and M. Dijkstra, Phys. Rev. Lett. **107**, 155501 (2011)

[47] X. Mao, Q. Chen, and S. Granick, Nat. Mater. **12**, 217 (2013)

[48] M. E. Davis, Nature **417**, 813 (2002)